AGU100 ADVANCING EARTH AND SPACE SCIENCE

Water Resources Research

RESEARCH ARTICLE
10.1029/2018WR023619

Key Points:
- A geometric description of free energy of a porous system with two immiscible fluids was found
- Geometric description of free energy in two-fluid flow is a function seven microscopic geometrically independent variables
- Using a thermodynamic approach, the amount of dissipated energy in drainage and imbibition processes was found

Supporting Information:
- Supporting Information S1

Correspondence to:
H. H. Khanamiri,
hamid.hosseinzade@ntnu.no

Citation:
Khanamiri, H. H., Berg, C. F., Slotte, P. A., Schlüter, S., & Torsæter, O. (2018). Description of free energy for immiscible two-fluid flow in porous media by integral geometry and thermodynamics. *Water Resources Research*, *54*, 9045–9059. https://doi.org/10.1029/2018WR023619

Received 9 JUL 2018
Accepted 23 OCT 2018
Accepted article online 29 OCT 2018
Published online 16 NOV 2018

Description of Free Energy for Immiscible Two-Fluid Flow in Porous Media by Integral Geometry and Thermodynamics

Hamid Hosseinzade Khanamiri[1], Carl Fredrik Berg[1], Per Arne Slotte[1], Steffen Schlüter[2], and Ole Torsæter[1]

[1]Department of Geoscience and Petroleum, PoreLab, Norwegian University of Science and Technology (NTNU), Trondheim, Norway, [2]Department of Soil System Sciences, Helmholtz-Centre for Environmental Research – UFZ, Halle, Leipzig, Germany

Abstract In integral geometry, intrinsic volumes are a set of geometrical variables to characterize spatial structures, for example, distribution of fluids in two-fluid flow in porous media. McClure et al. (2018, https://doi.org/10.1103/PhysRevFluids.3.084306) utilized this principle and proposed a geometric state function based on the intrinsic volumes. In a similar approach, we find a geometrical description for free energy of a porous system with two fluids. This is also an extension of the work by Mecke (2000, https://doi.org/10.1007/3-540-45043-2_6) for energy of a single fluid. Several geometrical sets of spatial objects were defined, including bulk of the two fluids, interfaces, and three-phase contact lines. We have simplified the description of free energy by showing how the intrinsic volumes of these sets are geometrically related. We obtain a description for energy as a function of seven microscopic geometrically independent variables. In addition, using a thermodynamic approach, we find an approximation for the free energy as a function of macroscopic parameters of saturation and pressure under quasi-static conditions. The combination of the two energy descriptions, by integral geometry and thermodynamics, completes the relation between the associated variables and enables us to find the unknown coefficients of the intrinsic volumes and to calculate the amount of dissipated energy in drainage and imbibition processes. We show that the theory is consistent with a set of experiments performed by Schlüter et al. (2016a, https://doi.org/10.1002/2015WR018254, 2017a, https://doi.org/10.1002/2016WR019815). However, in order to be more conclusive, it needs to be tested with larger data sets.

1. Introduction

Two-phase flow in porous media is typically described by the two macroscopic variables of pressure and saturation. In 1936, Wyckoff and Botset (1936) introduced the concept of relative permeability by generalization of Darcy's law (Darcy, 1856). The velocity (v_α) and pressure gradient (∇p_α) of fluid α are related by its relative permeability ($k_{r\alpha}$), as given in equation (1):

$$v_\alpha = -\frac{k_{r\alpha}(S_\alpha)k}{\mu_\alpha}\nabla p_\alpha, \tag{1}$$

where k, μ_α, and S_α are absolute permeability, viscosity, and saturation of fluid α, respectively. In this description, the relative permeability is assumed to be a function of saturation only. The same equation can be written for fluid β, and the pressures of two fluids (P_α and P_β) are connected by definition of a macroscopic capillary pressure (P_c), which is also assumed to be a function of saturation (Leverett, 1941):

$$P_c(S_\alpha) = P_\alpha - P_\beta. \tag{2}$$

The experimentally measured capillary pressure and relative permeabilities as functions of saturation often exhibit hysteresis; that is, the values of these parameters are different for drainage and imbibition (Jerauld & Salter, 1990; Joekar-Niasar et al., 2013; Killough, 1976; Smith et al., 1931). This means that the stated multiphase flow description above is physically incomplete (Hilfer, 1998). Niessner et al. (2011) stated that the extended Darcy's law for two-phase flow is compatible with a macroscale thermodynamically consistent approach under certain assumptions (Hassanizadeh & Gray, 1990).

In addition to hysteresis, relative permeabilities at similar saturations also depend on flow rate or capillary number (Tsakiroglou et al., 2015). Avraam and Payatakes (1995) observed that relative permeabilities

depended on microscopic flow regimes when the flow regime changed from ganglion dynamics to connected pathway. In addition to the saturation and flow regime, the relative permeability is affected by the geometrical distribution of the two fluid phases (Liu et al., 2017). These observations suggest that the microscopic phenomena, which affect the macroscopic outcome of the flow, have yet to be included in a general law for two-phase flow.

Due to the shortcomings of the traditional empirical description, researchers have proposed several alternative theories. Hassanizadeh and Gray (1993a) introduced capillary pressure dynamics by incorporating the rate of saturation changes into the capillary pressure function. The same authors believed that the main difference between single- and two-phase flow is the presence of fluid interfaces in two-phase flow (Gray & Hassanizadeh, 1991Hassanizadeh & Gray, 1993b). Therefore, they introduced interfacial area as an additional state variable (Hassanizadeh & Gray, 1993b). Further, Hilfer (1998) modified the generalized Darcy equations for two-phase flow by splitting the fluid saturations into percolating and nonpercolating and by incorporating the interfacial areas. His work resulted in macroscopic flow equations dependent on the microscopic flow regimes. Hilfer (2006a, 2006b) has also proposed a macroscopic phenomenological theory, again using percolating and nonpercolating fluid saturations as explicit state variables, but excluding the interfacial area in expense of a number of assumptions.

In recent years, microscopic characteristics of two-phase flow have been investigated in a number of experiments with increasingly improved spatial and temporal details, particularly using synchrotron X-ray computed microtomography (Armstrong et al., 2014; Bartels et al., 2017; Berg et al., 2013, 2015; Singh, Menke, et al., 2017; Singh, Scholl, et al., 2017). Herring et al. (2013) studied the influence of fluid topology on trapped nonwetting phase saturation by calculating the Euler characteristic (χ) of the nonwetting phase from X-ray microtomography images. In a number of recent works, Euler characteristic and in general fluid topology were utilized to characterize the pore scale phenomena (Armstrong et al., 2017; Herring et al., 2015; Khanamiri et al., 2017; Khanamiri & Torsæter, 2018; Liu et al., 2017; Rücker et al., 2015; Schlüter et al., 2016a, 2017a). These works suggest that Euler characteristic could be a missing state variable.

The Euler characteristic is a topological measure for studying the connectivity of spatial objects, for example, fluid clusters in porous media. It is also the integral of Gaussian curvature over the bounded surfaces (see Figure S2 in the supporting information). In integral geometry, the spatial objects in three dimensions can be geometrically characterized by four parameters of volume, surface area, integral of mean curvature, and integral of Gaussian curvature. These parameters are known as Minkowski functionals or intrinsic volumes (Klain, 1995). The characterization theorem in integral geometry states that certain physical properties of the spatial objects can be written as a linear combination of the intrinsic volumes (Hadwiger, 1957). Energy of a single fluid confined in porous media is an example of such physical properties (Mecke, 2000 and Mecke & Arns, 2005).

McClure et al. (2018) investigated which intrinsic volumes were required to describe the state of quasi-static two-phase flow in porous media. Further, they investigated constitutive relations among these parameters. Based on experimental and simulated microscopic fluid configurations, they proposed a state function between four intrinsic volumes of the nonwetting fluid. As the saturation and interfacial area represent two of the intrinsic volumes, their work is an extension of the previous research on the state variables (references above).

In this article, we expand on earlier work employing intrinsic volumes to describe two-phase flow. We attempt to find a geometrical description for free energy of a porous system with two fluids based on the microscopic intrinsic volumes under both extreme wetting and partial wetting conditions. Using a thermodynamic approach, we estimate the free energy based on the macroscopically measurable parameters under quasi-static conditions. Combining the energy estimated from the macroscopic parameters with the measured intrinsic volumes, we find a description for free energy by a linear combination of the intrinsic volumes. We will demonstrate this methodology on a set of experiments performed by Schlüter et al. (2016a, 2017a).

2. Theory

In this work, we assume that porous medium consists of a rigid solid and the pore space filled with two immiscible flowing fluids. We assume that the flow is quasi-static, that is, slow flow where the system is at

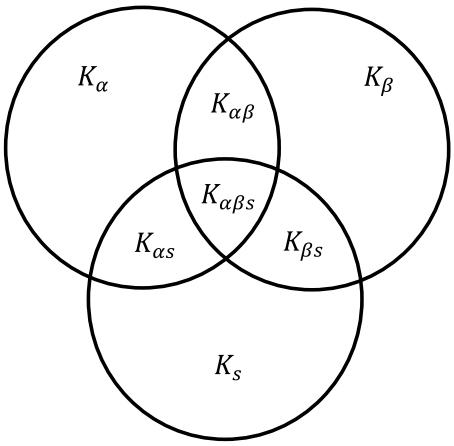

Figure 1. Conceptual illustration of the defined geometrical sets. K_α, K_β, and K_s represent fluids α and β and the solid, respectively; $K_{\alpha\beta}$, $K_{\alpha s}$, and $K_{\beta s}$ are the corresponding interfaces; and $K_{\alpha\beta s}$ are the three-phase contact lines.

hydraulic equilibrium. A relevant criterion for such a situation is low capillary number. The macroscopic capillary number (N_c) expresses the ratio of viscous to capillary forces. In this article, the macroscopic capillary number is defined as

$$N_c = \frac{\mu v}{\sigma}, \tag{3}$$

where v is the total Darcy velocity (macroscopic volumetric flux), μ is the invading fluid viscosity, and σ is the interfacial tension.

For flow in aquifers and oil reservoirs, the typical range of capillary numbers is 10^{-10}–10^{-6} (Dullien, 1992). The capillary number for transition from the quasi-static or capillary-dominated to viscous-dominated flow depends on the type of porous material. For instance, for a sandstone rock the transition occurs in the interval of 10^{-7}–10^{-6}, while it can be orders of magnitude higher for bead packs (Dullien, 1992). The thermodynamic estimation of energy, proposed in this work, is valid only for a quasi-static flow, while the geometrical description of energy is valid at both high and low capillary numbers.

2.1. Intrinsic Volumes

A short introduction on the necessary definitions in integral geometry is found in the supporting information. For a three-dimensional (3-D) set of objects K, for example, an assembly of fluid clusters with irregular shapes, let $V_0(\mathrm{K}) - V_3(\mathrm{K})$ denote the intrinsic volumes. This intrinsic volumes are equal to the volume (V), surface area (A), integral of mean curvature (H), and the integral of Gaussian curvature (χ) multiplied by constant coefficients, as shown in equations (4)–(7). The parameters κ_1 and κ_2 are the curvature terms, which are the inverse of the principal radii of curvature R_1 and R_2 for a surface element (dA).

$$V_0(K) = V(K), \tag{4}$$

$$V_1(K) = A(K) = \int_{\delta K} dA, \tag{5}$$

$$V_2(K) = H(K) = \frac{1}{2}\int_{\delta K}(\kappa_1 + \kappa_2)dA, \tag{6}$$

$$V_3(K) = \chi(K) = \frac{1}{4\pi}\int_{\delta K}\kappa_1\kappa_2 dA. \tag{7}$$

Mecke (2000) and Mecke and Arns (2005) employed integral geometry to describe the energy of a single fluid confined by a complex boundary. Considering the energy as a function of the geometry of the fluid, they argued that this energy function is continuous, additive, and invariant under rigid motion (see the supporting information). The energy function thereby fulfills the necessary conditions in Hadwiger's characterization theorem (Hadwiger, 1957); thus, the energy can be parameterized by a linear combination of the intrinsic volumes (Mecke & Arns, 2005):

$$F(K) = \Sigma_{i=0}^{n} c_i V_i(K), \tag{8}$$

where F is the energy of the set of objects K, the coefficients c_i are real numbers, and V_i are the intrinsic volumes, also known as Minkowski functionals.

In this article, we will extend the single-fluid description above to two immiscible fluids. Let the set of objects K_α be fluid α. We define sets K_β and K_s for the fluid phase β and the solid s in the same manner. The three sets $K_{\alpha\beta}$, $K_{\alpha s}$, and $K_{\beta s}$ represent the interfaces, where, for example, the set $K_{\alpha\beta}$ contains the interfaces of fluids α and β. Further, $K_{\alpha\beta s}$ represents the three phase contact lines. As the characterization theorem only holds for *compact* objects, we require that all objects contain their boundaries. Without the boundaries, the objects are not *closed* and therefore not *compact*. Thus, our set of objects K_α contains the interfaces $K_{\alpha\beta}$ of fluid α with fluid β; it also contains the interfaces $K_{\alpha s}$ of fluid α with the solid, s (see Figure 1). *Compactness* of $K_{\alpha\beta}$ requires that the three phase contact lines $K_{\alpha\beta s}$ are contained in this set. Similarly, the three phase contact lines $K_{\alpha\beta s}$ are also

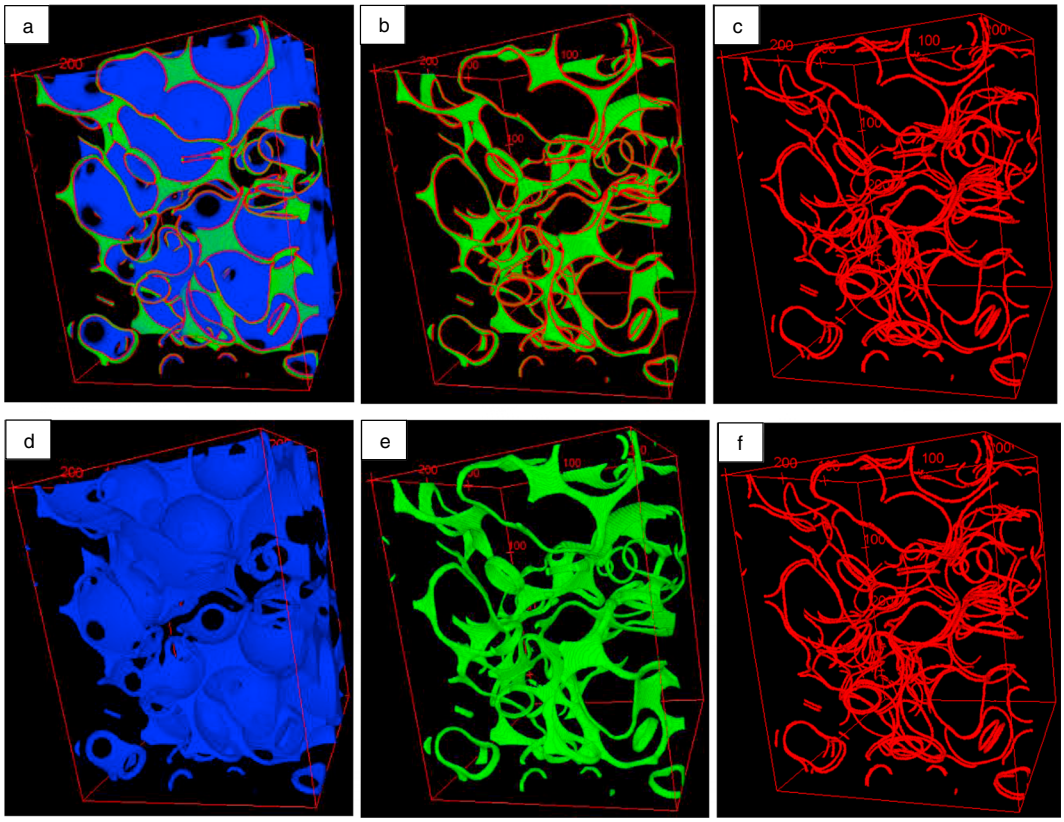

Figure 2. Experimental 3-D example of the defined geometrical sets and the constituent parts. The size of the cropped volume is 2,270 × 2,540 × 2,940 $(\mu m)^3$. In all figures, the solid and one of the fluids were removed to accentuate the examined fluid. (a) K_α contains the fluid α (blue), the interfaces of fluids α and β (green), and the three-phase contact lines (red); (b) $K_{\alpha\beta}$ contains interfaces of fluids α and β, and the three-phase contact lines; (c) $K_{\alpha\beta s}$ represents the three phase contact lines; (d–f) the corresponding constituents of K_α, $K_{\alpha\beta}$, and $K_{\alpha\beta s}$.

contained in $K_{\alpha s}$ and $K_{\beta s}$, and consequently in K_α, K_β and K_s, as visualized in Figure 1. All the defined sets are then *bounded* and *closed*, thereby they are all *compact*, as required by the characterization theorem. Experimental examples of these geometrical sets are shown in Figure 2.

In principle, a volume-free object does not have free energy. When we associate energy to a surface (or a line), it is the excess energy close to the surface relative to the energy in the bulk phases. For example, the energy associated with a fluid-fluid interface is the excess energy due to the arrangement and bonds between the molecules close to the interface relative to the arrangement and bonds between the molecules in the bulk phases. This excess energy is reflected in molar density gradients near the interface in an interval of typically few Angstroms to nanometers and can be described for instance by the density gradient theory (Adamson & Gast, 1997).

While it would be possible to treat the interfaces as 2-D surfaces and the contact lines as 1-D lines with an associated excess energy, we will follow another path in this article. As the interfaces are diffuse transitions from one phase to another, we will consider them as 3-D volumes of thickness ε, as illustrated in Figure 3. As the diffuse layer between two phases is in the molecular size range, the size of ε is in the order of nanometers. Similarly, the contact lines will be considered to have a circular cross section with a diameter of ε. The defined sets are therefore 3-D volumes (K_α, K_β, and K_s), 3-D surfaces ($K_{\alpha\beta}$, $K_{\alpha s}$, and $K_{\beta s}$), and 3-D lines ($K_{\alpha\beta s}$).

As the 3-D interface sets ($K_{\alpha\beta}$, $K_{\alpha s}$, and $K_{\beta s}$) have a volume proportional to ε (the thickness of an interface; see Figure 3), these volumes can be ignored, because ε is approximately 3 orders of magnitude smaller than the other length scales in porous media, for example, length scale associated with curvature of fluid-fluid interfaces. Further, the surface of the 3-D interface sets is composed of two sides and the additional bounding three-phase contact line. In the limit $\varepsilon \to 0$, the two sides converge to the same surface area. These sides

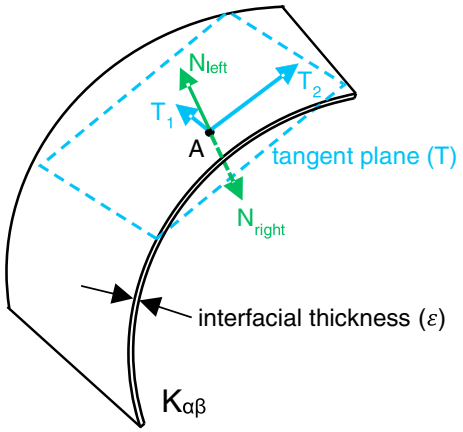

Figure 3. Plane T is tangent to the interface of fluids α and β ($K_{\alpha\beta}$) at an arbitrary point A. The principal tangent vectors are T_1 and T_2, and N_{left} and N_{right} symbolize the unit normal vectors on the left and right sides of the interface, respectively. Having T_1' and T_2' as the derivatives of T_1 and T_2, the principal curvature $\kappa_{1,\text{ left}}$ can be obtained from $T_1' = \kappa_{1,\text{left}} N_{\text{left}}$, while $\kappa_{1,\text{ right}}$ can be obtained using $T_1' = \kappa_{1,\text{right}} N_{\text{right}}$. The opposite sign of the unit normal vectors ($N_{\text{left}} = -N_{\text{right}}$) results in $\kappa_{1,\text{ left}} = -\kappa_{1,\text{ right}}$. Similarly, one can also show $\kappa_{2,\text{ left}} = -\kappa_{2,\text{ right}}$. The same absolute value but opposite sign for the curvatures on the two sides of interface leads to the simplification of integral of mean curvature, $V_{2\alpha\beta,\text{ left}} = -V_{2\alpha\beta,\text{ right}}$, and integral of Gaussian curvature, $V_{3\alpha\beta,\text{ left}} = V_{3\alpha\beta,\text{ right}}$, for the interfacial sets in equation (9).

have the same absolute values, but opposite signs, for the curvatures (see Figure 3). The integral of mean curvature and Gaussian curvature for a 3-D interface set is therefore split into left, right, and the bounding line of the interface and simplified using the relation of curvatures in different domains. Interestingly, the integration shows that the integral of mean curvature for the interfaces is proportional to the length of the three-phase contact lines ($L_{\alpha\beta s}$), as seen in equation (9) below.

$$
\begin{aligned}
&V_{0\alpha\beta} = \mathcal{O}(\varepsilon),\ \ V_{0\alpha\beta}\to 0 \ \text{ when } \ \varepsilon\to 0\\
&V_{1\alpha\beta} = A_{\alpha\beta}\\
&V_{2\alpha\beta} = V_{2\alpha\beta,\text{left}} + V_{2\alpha\beta,\ \text{right}} + V_{2\alpha\beta,\ \text{line}}\\
&\quad = -V_{2\alpha\beta,\ \text{right}} + V_{2\alpha\beta,\ \text{right}} + \frac{1}{2}\int_{\delta K_{\alpha\beta s}}\left(\frac{1}{R_1} + \frac{1}{R_{2\to\infty}}\right)dA\\
&\quad = \frac{1}{2}\int_{\delta K_{\alpha\beta s}}\frac{dA}{R_1} = \frac{1}{2}\int_{L_{\alpha\beta s}}\frac{\frac{\pi}{2}dL}{\frac{\varepsilon}{2}} = \frac{\pi}{2}L_{\alpha\beta s}\\
&V_{3\alpha\beta} = V_{3\alpha\beta,\text{left}} + V_{3\alpha\beta,\ \text{right}} + V_{3\alpha\beta,\ \text{line}} = 2V_{3\alpha\beta,\ \text{right}} + V_{3\alpha\beta,\ \text{line}}\\
&\quad = 2\frac{1}{4\pi}\int_{\delta K_{\alpha\beta}}\frac{1}{R_1 R_2}dA + \frac{1}{4\pi}\int_{\delta K_{\alpha\beta s}}\frac{1}{(R_1)(R_{2\to\infty})}dL = \frac{1}{2\pi}\int_{\delta K_{\alpha\beta}}\frac{1}{R_1 R_2}dA.
\end{aligned}
\tag{9}
$$

For the second last equality in the derivation of $V_{2\alpha\beta}$ we go from integrating over the surface to an integral along the three-phase contact line. The surface $\delta K_{\alpha\beta s}$ here is considered to have a half-circle cross section with a radius $\varepsilon/2$ along the contact line.

Similar to the 3-D interface sets, the intrinsic volumes for the 3-D three-phase contact lines are simplified below. In line with the derivation above, the contact lines are assumed to have a circular cross section with a radius of $\varepsilon/2$.

$$
\begin{aligned}
&V_{0\alpha\beta s} = \mathcal{O}\left(\varepsilon^2\right),\ \ V_{0\alpha\beta s}\to 0 \ \text{ when } \ \varepsilon\to 0\\
&V_{1\alpha\beta s} = \mathcal{O}(\varepsilon),\ \ V_{1\alpha\beta s}\to 0 \ \text{ when } \ \varepsilon\to 0\\
&V_{2\alpha\beta s} = \frac{1}{2}\int_{\delta K_{\alpha\beta s}}\left(\frac{1}{R_1} + \frac{1}{R_{2\to\infty}}\right)dA = \frac{1}{2}\int_{\delta K_{\alpha\beta s}}\frac{dA}{R_1} = \frac{1}{2}\int_{L_{\alpha\beta s}}\frac{\frac{2\pi}{2}dL}{\frac{\varepsilon}{2}} = \pi L_{\alpha\beta s}\\
&V_{3\alpha\beta s} = \int_{\delta K_{\alpha\beta s}}\frac{1}{(R_1)(R_{2\to\infty})}dA = 0.
\end{aligned}
\tag{10}
$$

Note that we assume the volume and surface area of the three-phase contact lines can be ignored for small ε. Further, the Euler characteristic approaches 0 as one of the curvature terms approaches 0. This is in agreement with the fact that a contact line fully inside the observed medium is topologically equivalent to a torus, which has an Euler characteristic of 0.

2.2. Geometrical Description of Free Energy

In this section, we attempt to express the total free energy of the system, F, in terms of the energy of its constituent geometrical sets K_α, K_β, K_s, $K_{\alpha\beta}$, $K_{\alpha s}$, $K_{\beta s}$, and $K_{\alpha\beta s}$ as defined in the previous section. Let F_i symbolize the free energy of the set K_i. The entire system is contained in the K_α, K_β, and K_s; however, these sets contain the interface sets $K_{\alpha\beta}$, $K_{\alpha s}$, and $K_{\beta s}$ twice, as illustrated in Figure 1. Thus, the sum of the energies $F_s + F_\alpha + F_\beta$ would include the free energy of the interface sets $F_{\alpha\beta} + F_{\alpha s} + F_{\beta s}$ twice. These must therefore be subtracted, as shown in equation (11) below. Further, as the energy of three phase contact lines has been added 3 times with the phases and subtracted 3 times with the interfaces, it must be added to balance the total free energy as follows:

$$F = F_s + F_\alpha + F_\beta - F_{\alpha\beta} - F_{\alpha s} - F_{\beta s} + F_{\alpha\beta s}. \tag{11}$$

The individual energy terms in the right-hand side of equation (11) can be expanded using equation (8) and the intrinsic volumes of the defined sets.

$$F = F_s + \Sigma_{i=0}^{3} c_{i\alpha} V_{i\alpha} + \Sigma_{i=0}^{3} c_{i\beta} V_{i\beta} - \Sigma_{i=0}^{3} c_{i\alpha\beta} V_{i\alpha\beta} - \Sigma_{i=0}^{3} c_{i\alpha s} V_{i\alpha s} - \Sigma_{i=0}^{3} c_{i\beta s} V_{i\beta s} + \Sigma_{i=0}^{3} c_{i\ \alpha\ \beta s} V_{i\ \alpha\ \beta s}. \tag{12}$$

Here we do not expand the energy for the solid, as this will remain constant for our systems.

The purpose of the remainder of this section is to find the independent intrinsic volumes. The free energy is a function of temperature for incompressible systems; that is, the c_i coefficients in equation (12) are constant for an isothermal process.

A number of the variables in equation (12) are geometrically dependent. We will show that there are seven geometrically independent intrinsic volumes: one fluid volume (or saturation), two areas, integral of mean curvature of one of the fluid phases, two integrals of Gaussian curvature (Euler characteristic), and the length of three-phase contact lines. This will result in the following equations:

$$F = F_0 + \widehat{c}_0 S_\alpha V + \widehat{c}_{1\alpha} V_{1\alpha} + \widehat{c}_{2\alpha} V_{2\alpha} + \widehat{c}_{3\alpha} V_{3\alpha} + \widehat{c}_{1\beta} V_{1\beta} + \widehat{c}_{3\beta} V_{3\beta} + \widehat{c}_{\alpha\beta s} V_{2\alpha\beta s,} \tag{13}$$

$$\widehat{F} = \widehat{F}_0 + \widehat{c}_0 S_\alpha + \widehat{c}_{1\alpha} \widehat{A}_\alpha + \widehat{c}_{2\alpha} \widehat{H}_\alpha + \widehat{c}_{3\alpha} \widehat{\chi}_\alpha + \widehat{c}_{1\beta} \widehat{A}_\beta + \widehat{c}_{3\beta} \widehat{\chi}_\beta + \widehat{c}_{\alpha\beta s} \widehat{L}_{\alpha\beta s}. \tag{14}$$

In equation (14), both sides of equation (13) were divided by the total volume of the system (V) to express the intrinsic volumes and free energy as intensive variables. The symbols of the intrinsic volumes were also converted to the typical ones used in equations (4)–(7) for convenience. The symbol S_α in equation (14) is the saturation of fluid α.

The first step in the process of eliminating dependent variables is substitution of equations (9) and (10) into equation (12):

$$F = F_s + \Sigma_{i=0}^{3} c_{i\alpha} V_{i\alpha} + \Sigma_{i=0}^{3} c_{i\beta} V_{i\beta} - \sum_{i=1,3} c_{i\alpha\beta} V_{i\alpha\beta} - \sum_{i=1,3} c_{i\alpha s} V_{i\alpha s} - \sum_{i=1,3} c_{i\beta s} V_{i\beta s} + \widehat{c}_{\alpha\beta s} L_{\alpha\beta s}. \tag{15}$$

For the interfaces the summation $\Sigma_{i\,=\,1,\,3}$ indicates that the sum runs over indices 1 and 3. The index 2 is proportional to the length of the contact line ($L_{\alpha\beta s}$) and has therefore been included in the last term. There were in total four terms with the length of the three-phase contact lines, and the constant coefficient for this variable is simply changed to $\widehat{c}_{\alpha\beta s}$ in equation (15). The resulting equation (15) has 13 intrinsic volumes, which will be reduced to seven in the following.

The sum of the volumes of the two phases ($V_{0\alpha}$ and $V_{0\beta}$) equals a constant pore volume. Therefore, the two volumes can be expressed by means of saturation S_α of the fluid α:

$$\begin{aligned} V_{0\alpha} &= S_\alpha \varphi V \\ V_{0\beta} &= (1 - S_\alpha)\varphi V, \end{aligned} \tag{16}$$

where φ and V are the constant porosity and total volume of the system, respectively. The new term S_α, which replaces the $V_{0\alpha}$ and $V_{0\beta}$ terms in equation (15), takes a coefficient $\widehat{c}_0$:

$$\widehat{c}_0 = \varphi\left(c_{0\alpha} - c_{0\beta}\right). \tag{17}$$

The interfacial areas $V_{1\alpha s}$, $V_{1\beta s}$, and $V_{1\alpha\beta}$ can be expressed from the areas $V_{1\alpha}$, $V_{1\beta}$, and V_{1s} as follows:

$$\begin{aligned} V_{1\alpha} - V_{1\beta} + V_{1s} &= V_{1\alpha s} \\ V_{1\beta} - V_{1\alpha} + V_{1s} &= V_{1\beta s} \\ V_{1\alpha} + V_{1\beta} - V_{1s} &= V_{1\alpha\beta}. \end{aligned} \tag{18}$$

Here we use the symmetry rule of $V_{1ij} = V_{1ji}$. Thus, $V_{1\alpha s}$, $V_{1\beta s}$, and $V_{1\alpha\beta}$ can be eliminated by inserting equation (18) into equation (15) and updating the coefficients of $V_{1\alpha}$ and $V_{1\beta}$ as follows.

$$\begin{aligned}\widehat{c}_{1\alpha} &= c_{1\alpha} + c_{1\alpha s} - c_{1\beta s} + c_{1\alpha\beta}\\ \widehat{c}_{1\beta} &= c_{1\beta} - c_{1\alpha s} + c_{1\beta s} + c_{1\alpha\beta}.\end{aligned} \tag{19}$$

The multiplication of coefficients in V_{1s} is constant, and they can be accumulated in a single coefficient, adding up to F_s in equation (13).

The integrated Gaussian curvature (V_3) have the same symmetry and summation rule as for the areas and would therefore yield similar expressions as in equation (18). Similar to the coefficients for the areas in equation (19), we can eliminate $V_{3\alpha s}$, $V_{3\beta s}$, and $V_{3\alpha\beta}$ in equation (15) by updating the coefficients for $V_{3\alpha}$ and $V_{3\beta}$ as

$$\begin{aligned}\widehat{c}_{3\alpha} &= c_{3\alpha} + c_{3\alpha s} - c_{3\beta s} + c_{3\alpha\beta}\\ \widehat{c}_{3\beta} &= c_{3\beta} - c_{3\alpha s} + c_{3\beta s} + c_{3\alpha\beta}.\end{aligned} \tag{20}$$

As illustrated in Figure 3, the integrated mean curvature (V_2) have the following symmetry:

$$V_{2\alpha\beta} = -V_{2\beta\alpha.} \tag{21}$$

As a result,

$$V_{2\alpha} + V_{2\beta} = V_{2\alpha s} + V_{2\alpha\beta} + V_{2\beta s} + V_{2\beta\alpha} = V_{2\alpha s} + V_{2\beta s} = -V_{2s}. \tag{22}$$

The term V_{2s} is constant. Therefore, $V_{2\alpha}$ and $V_{2\beta}$ are dependent. Using equation (22), we can replace $V_{2\beta}$ in equation (15) by updating the coefficient of $V_{2\alpha}$ with the following new coefficient:

$$\widehat{c}_{2\alpha} = c_{2\alpha} - c_{2\beta.} \tag{23}$$

Finally, inserting equations (16)–(20), (22), and (23) into equation (15) results in equation (13) as a description for free energy as a function of seven geometrically independent variables.

In the reduction of variables above, we chose some of the intrinsic volumes over the others. The choices could be different because of the symmetry. The choice of variables is to a large degree arbitrary. The important point is that the geometrically independent variables are a group of one volume (or saturation), two areas, the integral of mean curvature of one of the fluid phases, two integrals of Gaussian curvature (Euler characteristic), and the length of three-phase contact lines.

2.3. Geometrical Description of Free Energy in Extreme Wetting Conditions

In extreme wetting conditions, it is assumed that the solid surfaces are almost always coated by a film of the wetting fluid (Abdallah et al., 2007), and the nonwetting fluid does not have any contact with the solid surfaces. In the equations in previous section, we assume that α and β are the nonwetting and wetting fluids, respectively, and we replace the subscripts α with n (nonwetting) and β with w (wetting). In extreme wetting conditions, we will have $V_{\mathrm{ins}} = 0$ for all i. Implementing the same simplifications as in the previous section results in equation (24) for surface area and integral of Gaussian curvature:

$$\begin{aligned}V_{1\mathrm{w}} &= V_{1\mathrm{n}} + V_{1\mathrm{s}}\\ V_{3w} &= V_{3n} + V_{3s}.\end{aligned} \tag{24}$$

According to equation (24), areas and integrals of Gaussian curvature for the wetting and nonwetting fluids are dependent. These dependencies result in one independent surface area and one independent integral of Gaussian curvature. Keeping these two intrinsic variables for the nonwetting phase with the following coefficients enables us to remove the corresponding variables for the wetting phase in equation (14).

$$\begin{aligned}\overline{c}_{1\mathrm{n}} &= \widehat{c}_{1\mathrm{n}} + \widehat{c}_{1\mathrm{w}}\\ \overline{c}_{3n} &= \widehat{c}_{3n} + \widehat{c}_{3w}\end{aligned}. \tag{25}$$

In addition, the three-phase contact lines disappear when the nonwetting phase does not have any contact with the solid surfaces. Therefore, equation (14) can be reduced to only four independent variables:

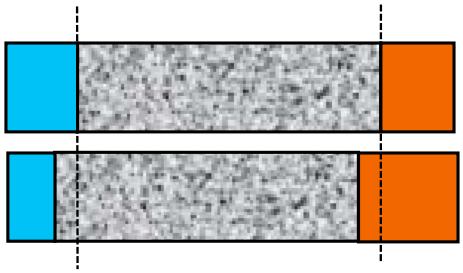

Figure 4. External work is associated with the volume changes in the fluid reservoirs to the left and right of the porous medium: $dV_w = -dV_n$. Since the total volume of each phase is preserved, the same volume changes apply with opposite sign to the volumes in the porous medium: $dS_w = -dV_w/(\phi V)$.

$$\widehat{F} = \overline{F}_0 + \widehat{c}_0 S_n + \overline{c}_{1n}\widehat{A}_n + \widehat{c}_{2n}\widehat{H}_n + \overline{c}_{3n}\widehat{\chi}_n. \tag{26}$$

Again, it should be noted that the choice of intrinsic volumes in equation (26) is arbitrary as long as there is exactly one volume (saturation), one area, integral of mean curvature of one of the fluid phases, and one Euler characteristic in the geometrical description of free energy.

2.4. Thermodynamic Description of Energy

In the previous sections, the energy of the porous system was formulated based on geometrical parameters in equations (14) and (26). In this section, we will apply a simple thermodynamic approach following Leverett (1941) and Morrow (1970).

When the two phases, wetting (w) and nonwetting (n), enter and leave the porous medium at different pressures, P_w and P_n(see Figure 4), the surrounding apply the following external work (W_{external}) on the system:

$$dW_{\text{external}} = P_w dV_w + P_n dV_n = (P_w - P_n)dV_w = -P_c dV_w = -\phi V P_c dS_w, \tag{27}$$

where we have assumed incompressible fluids and we have used the symbol P_c for the pressure difference. The pressure difference P_c is conventionally identified with the macroscopic capillary pressure; the present analysis does however not rely on this identification.

We have disregarded gravity, which is fair for small core samples; however, gravity could be included without loss of generality.

For an isothermal reversible process the applied work is equal to the change in the Helmholtz free energy F, and in an irreversible process some energy will also be dissipated

$$dW_{\text{external}} = dF + dE_{\text{dissipated.}} \tag{28}$$

Under the assumption of slow displacement, the viscous dissipation due to the macroscopic flow is negligible. However, as a result of the saturation changes during displacement, metastable fluid configurations are created. The relaxation of these states induces microscopic viscous fluid flow, called Haines jumps (Haines, 1930). These Haines jumps are fast irreversible local processes causing energy dissipation. As a consequence, the integral of the capillary pressure yields an upper bound for the (positive) free energy change in the system for drainage and a lower bound for the (negative) free energy change during imbibition. We define the displacement efficiency for drainage as the fraction of the applied work that is stored as free energy:

$$E_D = \frac{dF}{dW} = -\frac{1}{\phi V P_c}\frac{dF}{dS_w}. \tag{29}$$

Similarly, we define the efficiency for imbibition as the fraction of released free energy that is delivered as work:

$$E_I = -\frac{dW}{dF} = \phi V P_c \frac{dS_w}{dF}. \tag{30}$$

The efficiencies are not expected to be constant throughout the process.

Morrow (1970) conducted experiments to investigate the efficiency of different displacement processes and defined the displacement efficiency for drainage as the fraction of the total applied work that is stored as free energy:

$$\overline{E}_D = \frac{\Delta F}{W} = \frac{\Delta F}{-\phi V \int P_c dS_w}. \tag{31}$$

If E_D is constant we have $\overline{E}_D = E_D$, so that $\overline{E}_D$ can be interpreted as an average efficiency. Morrow defined the total efficiency of imbibition as

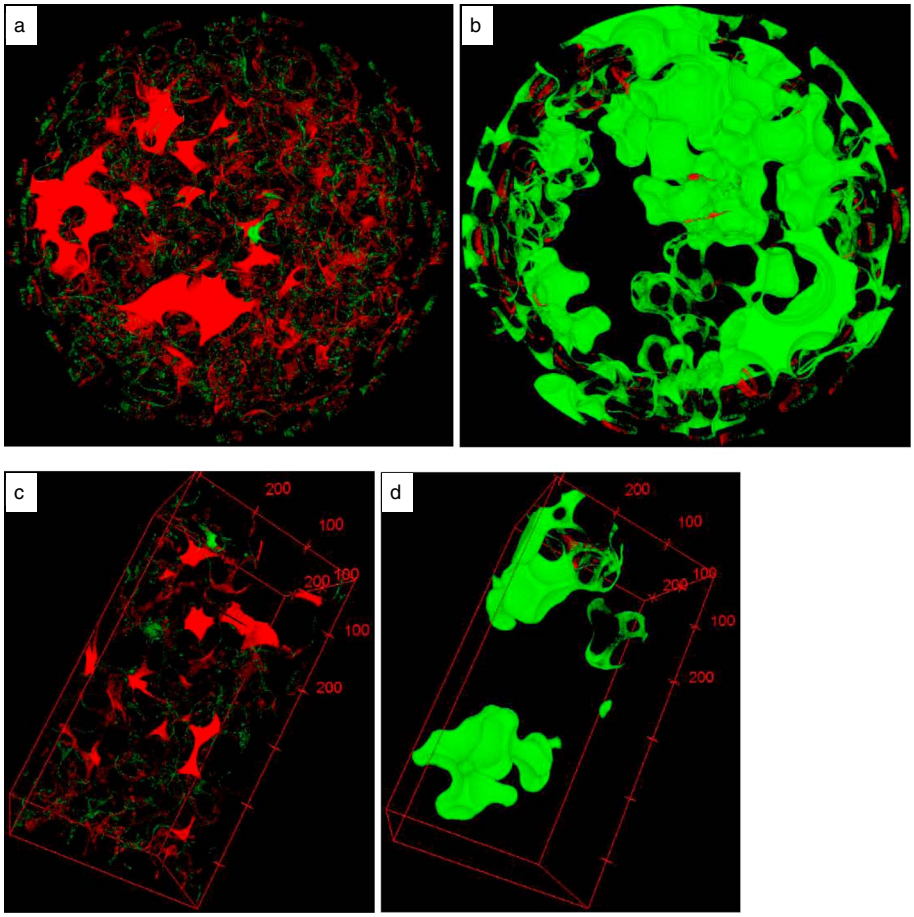

Figure 5. Experimental examples of (a) main imbibition and (b) primary drainage. The volume is 6,308 × 6,308 × 4,838 $(\mu m)^3$ in both (a) and (b); the red color represents the parts of pore space where the wetting fluid has replaced the non-wetting in two consecutive time steps, whereas the green color represents the opposite for the same time steps. All the unchanged voxels are masked. The figures (c) and (d) are smaller volumes, 2,587 × 1,982 × 4,838 $(\mu m)^3$, cropped from (a) and (b), respectively.

$$\bar{E}_I = \frac{W + \Delta F_0}{\Delta F_D}, \tag{32}$$

where W is the delivered work, ΔF_0 is the remaining stored free energy at the end of imbibition, and ΔF_D is the stored energy at the end of drainage. Morrow's definition of total efficiency of imbibition has no direct connection to our definition. In his experiments, he estimated the free energy changes based on measuring surface areas and known interfacial tension σ_{nw} and contact angle θ:

$$F = \sigma_{nw}(A_{nw} + A_{ns}\cos\theta). \tag{33}$$

The experiments were conducted on bead packs filled with a blue dyed epoxy, and then displaced by air under gravity. After hardening, the sample was filled with an orange epoxy to strengthen the sample. In order to calculate the total surface areas, and the corresponding applied work as an integral over capillary pressure, thin sections were made from different heights corresponding to different saturations and capillary pressures.

According to Morrow (1970), the imbibition process had an efficiency of 92.5%, compared to an efficiency of 79% for primary drainage (PD) and 77.5% for secondary drainage.

In Figure 5, we have visualized examples of changes in fluid geometry during main imbibition (MI) and PD. These examples suggest that the majority of the displacement events in the MI is in the form of change in

the wetting films (thinning/thickening), while the majority of events in the PD are centralized in the pore bodies. For the PD, the nonwetting fluid has to overcome the required capillary pressure at the pore entries, resulting in Hains jumps and consequently dissipation of energy. For the MI, swelling or thinning of wetting films is assumed closer to a reversible process and therefore will dissipate less energy. Consequently, the MI is expected to have higher efficiency than the PD, in line with the experimental results from Morrow (1970).

3. Experimental Examples

In this section, the developed theory is tested for a number of experiments performed by Schlüter et al. (2016a, 2017a) using synchrotron-based X-ray microtomography of two-fluid displacement at quasi-static conditions. We use the available data of a number of experiments performed on a porous cylindrical sample (diameter of 5.8 mm and height of 7 mm) made of sintered soda lime glass beads (35% 0.6 mm, 35% 0.8 mm, and 30% 1.0–1.4 mm diameter). Configuration of fluids was captured using synchrotron X-ray computed microtomography during the experiment.

A full cycle of PD, MI, and main drainage (MD) experiments were performed using brine (1:6 mass ratio between CsCl and water) as the wetting fluid and n-dodecane as the nonwetting fluid. The bottom of the sample was connected to a syringe pump with a brine reservoir, and the top was connected to a dodecane reservoir at atmospheric pressure. The experiments were performed at very slow flow rates with a capillary number of 10^{-8}, keeping the fluids at quasi-static equilibrium. Details of the experiments and the URL address to access the data are listed in the references (Schlüter et al., 2016a, 2016b).

In addition, four spontaneous imbibition experiments (A, B, C1, and C2) were performed after fast drainage, where C2 is a repetition of experiment C1. The macroscopic capillary number for the fast drainage experiments where A: 3×10^{-7}, B: 3×10^{-6}, and C1 and C2: 3×10^{-5}. Spontaneous imbibition experiments were performed after the fast injection stopped, and the interfaces had been allowed to relax toward a new equilibrium state. The macroscopic capillary number for the imbibition experiments was in the order of 10^{-10}. Given the low capillary number, these cases resemble quasi-static conditions. Details of the experiment are available at Schlüter et al. (2017a), and the URL address to access the data is listed in the references (Schlüter et al., 2017b).

Schlüter et al. (2017a) estimated contact angle of 42°, which falls approximately in the range of the water wet systems rather than the strongly water wet ones. We will therefore use equation (14) in the following as the geometric description of the free energy. However, the experiments were performed at a wettability close to strongly water wet. Given the smaller number of free parameters needed for describing an extreme wetting case (equation (26)), this could imply that some of the geometric parameters in equation (14) would be intercorrelated.

The intrinsic volumes were calculated using QuantIm (Vogel et al., 2010) and ImageJ (Rasband, 1997–2016) on the segmented images published by Schlüter et al. (2016b, 2017b). The two independent calculations resulted in the same values for volumes, surface areas, and Euler characteristics with a six-neighborhood arrangement for every pixel. Euler characteristics with a 26-neighborhood arrangement were slightly different in the two calculations, probably because they handle the boundaries differently. We therefore selected the Euler characteristics with the 6-neighborhood arrangement for further analysis. We calculated the integral of mean curvature for the nonwetting phase by QuantIm only. The length of three-phase contact lines was calculated using ImageJ by extraction and skeletonization of the edges of solid, wetting, and nonwetting fluids.

Based on visual observation of the changes in fluid configuration in Figure 5, and the results from Morrow (1970), we assume that the spontaneous imbibition process is close to reversible with an efficiency of 0.925:

$$d\widehat{F} \simeq -0.925 \int \phi P_c dS_w = 0.925 \int \phi P_c dS_n. \tag{34}$$

It should be noted that changing the efficiency to 1 has a small impact on the following results. We used the four spontaneous imbibition experiments and the spontaneous part of the MI to fit the adjustable parameters in equation (26).

As we do not have the energy for the starting point of the five imbibition processes, these are treated as unknowns. Together with the seven parameters in equation (14), this yields a total of 12 adjustable parameters. We then have the following equations for the five processes:

$$\Delta\widehat{F}(S_n) = 0.925\int_{S_i}^{S_n}\phi P_c dS_n, \tag{35}$$

$$\Delta\widehat{F}(S_n) = \widehat{c}_0 S_n + \widehat{c}_{1n}\widehat{A}_n + \widehat{c}_{2n}\widehat{H}_n + \widehat{c}_{3n}\widehat{\chi}_n + \widehat{c}_{1w}\widehat{A}_w + \widehat{c}_{3w}\widehat{\chi}_w + \widehat{c}_{wns}\widehat{L}_{wns} - \widehat{F}_i. \tag{36}$$

Here S_i is the initial nonwetting saturation and $\widehat{F}_i$ is the initial energy at the beginning of each of the five imbibition processes.

In the following we show how focusing on the physical meaning of the coefficients can lead to a more robust regression for the adjustable parameters. Let the interfacial tension between the fluids α and β be defined as the derivative of the free energy with respect to the interface area ($A_{\alpha\beta}$). We assume that the interfacial tension between the two fluids ($\sigma_{\alpha\beta}$) is measured. We further assume that the solid consists of a single mineral, and the fluids have few components that can alter the wettability of the surface and that the contact angle (θ) for the fluids α and β and the solid phase is measured out of porous material. Under these assumptions, the coefficients $\widehat{c}_{1n}$ and $\widehat{c}_{1w}$ in equation (36), and in general the coefficients $\widehat{c}_{1\alpha}$ and $\widehat{c}_{1\beta}$ in equation (14), are

$$\begin{aligned}\widehat{c}_{1\alpha} &= \frac{1}{2}(1 - cos\ \theta)\sigma_{\alpha\beta}\\ \widehat{c}_{1\beta} &= \frac{1}{2}(1 + cos\ \theta)\sigma_{\alpha\beta}.\end{aligned} \tag{37}$$

Consequently, if both $\sigma_{\alpha\beta}$ and θ are measured independent from the flooding experiments, then the number of regression parameters can be reduced by two. If only $\sigma_{\alpha\beta}$ is measured, the number of regression parameters can still be reduced by one, using the following relationship:

$$\widehat{c}_{1\alpha} = \sigma_{\alpha\beta} - \widehat{c}_{1\beta.} \tag{38}$$

We will now derive the above expressions. The free energy for a macroscopic droplet on a flat solid surface is conventionally expressed using interfacial tensions as

$$\widehat{F}_A = \sigma_{\alpha\beta}\frac{\widehat{A}_{\alpha\beta}}{2} + \sigma_{\alpha s}\frac{\widehat{A}_{\alpha s}}{2} + \sigma_{\beta s}\frac{\widehat{A}_{\beta s}}{2}. \tag{39}$$

The volumes of the fluids α and β are constant; we therefore ignore them in equation (39) without loss of generality. The fraction $(\frac{1}{2})$ appears in equation (39) because of double-counting of the areas in the definition of the Minkowski functionals for the interfacial objects ($K_{\alpha\beta}$, $K_{\alpha s}$, $K_{\beta s}$). The total solid area is constant, and we have

$$A_s = \frac{A_{\alpha s}}{2} + \frac{A_{\beta s}}{2}. \tag{40}$$

Using equation (40), we may eliminate $A_{\beta s}$ from equation (39).

$$\widehat{F}_A = \sigma_{\alpha\beta}\frac{\widehat{A}_{\alpha\beta}}{2} + \left(\sigma_{\alpha s} - \sigma_{\beta s}\right)\frac{\widehat{A}_{\alpha s}}{2} + \sigma_{\beta s}\widehat{A}_s. \tag{41}$$

In our theory (equation (14) or equation (36)), the free energy contains additional terms related to surface curvature and contact line length ($\widehat{H}_n, \widehat{\chi}_n, \widehat{\chi}_w, \widehat{L}_{wns}$), but for a macroscopic droplet these contributions can be ignored so that the free energy is

$$\widehat{F}_A = \widehat{c}_{1\alpha}\widehat{A}_\alpha + \widehat{c}_{1\beta}\widehat{A}_{\beta.} \tag{42}$$

Similar to equation (40), we have

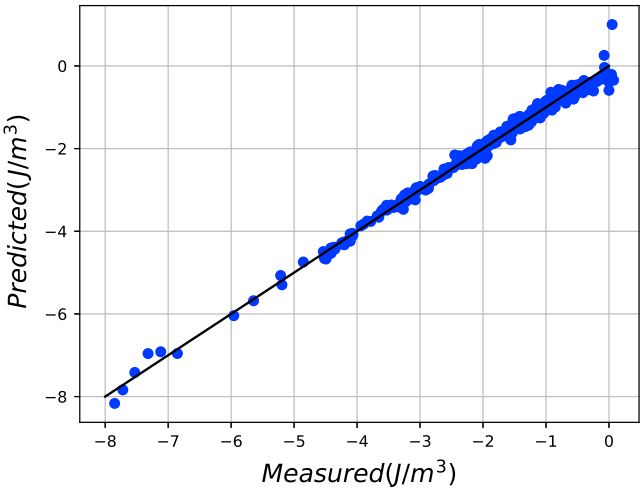

Figure 6. The resulted crossplot after adjusting the 11 free parameters in equation (36) by a least squares linear regression. The external work given by equation (35) is on the *x* axis, and the change in free energy calculated by the geometrical parameters given by equation (36) is on the *y* axis. Equation (38) was used to reduce the number of regression parameters by 1.

$$A_\alpha = \frac{A_{\alpha s}}{2} + \frac{A_{\alpha\beta}}{2}$$
$$A_\beta = \frac{A_{\beta s}}{2} + \frac{A_{\alpha\beta}}{2} = A_s - \frac{A_{\alpha s}}{2} + \frac{A_{\alpha\beta}}{2}. \tag{43}$$

Inserting equation (43) into equation (42) results in the following description for the free energy:

$$F_A = \frac{1}{2}\left(\hat{c}_{1\alpha} + \hat{c}_{1\beta}\right)\hat{A}_{\alpha\beta} + \frac{1}{2}\left(\hat{c}_{1\alpha} - \hat{c}_{1\beta}\right)\hat{A}_{\alpha s} + \hat{c}_{1\beta}\hat{A}_s. \tag{44}$$

Comparing equations (41) and (44) gives

$$\hat{c}_{1\alpha} + \hat{c}_{1\beta} = \sigma_{\alpha\beta}$$
$$\hat{c}_{1\alpha} - \hat{c}_{1\beta} = \sigma_{\alpha s} - \sigma_{\beta s} = \sigma_{\alpha\beta}\cos\,\theta. \tag{45}$$

In principle, the coefficients $\hat{c}_{1\alpha}$ and $\hat{c}_{1\beta}$ remain the same when we switch from a flat solid surface accommodating fluids α and β on itself (equation (44)) to a porous solid containing the same fluids (equation (36)), given that the chemical compositions of fluids and solid have not altered. Therefore, the coefficients $\hat{c}_{1\alpha}$ and $\hat{c}_{1\beta}$ for the porous solid can be obtained from the simplified separate measurements, that is, typical contact angle and interfacial tension measurements.

There is no independent contact angle measurement for the experimental data, but the measured interfacial tension is 36×10^{-3} J/m^2. Therefore, we use equation (38) to reduce the number of regression parameters by 1. The 11 adjustable parameters in equation (36) were estimated using the *python* package *statsmodels* for ordinary least squares linear regression (Seabold & Perktold, 2010). The regression resulted in a good fit between the prediction and the measurement (see Figure 6). The resulted regression parameters, employing equation (45), give a contact angle of 43°. This is comparable with the values 30°–60° reported by Schlüter et al. (2017a) for the same data sets.

The adjustable parameters are highly correlated; thus, the resulting parameters are not considered robust. The number of data points is limited for fitting the large number of adjustable parameters. This can be seen in Figure 7, where the intrinsic volumes are plotted versus saturation. Note that the data for the MI do not cover the nontrivial curvature for the PD and MD curves at low saturations. A data set with less correlation between the intrinsic volumes is expected to yield more robust results.

In Figure 8, we have plotted the external work for the bounding flooding sequence, that is, PD, MI, and MD, versus the free energy calculated by the geometrical parameters in equation (36). Following equation (28), for a reversible process the amount of dissipated energy reduces to 0; thus, the plotted curve would follow a 1–1 line. We observe that the spontaneous part of the imbibition process is close to 1–1, in agreement with the regression plotted in Figure 6. We also observe that the starts of the two drainage curves seem to have less dissipated energy than the latter parts. This could be interpreted as fewer irreversible processes early in the drainage, likely because the nonwetting phase has not yet developed a large interfacial area where the irreversible processes are expected to happen (see Figure 7).

The latter part of each drainage shows a decrease in free energy when external work is applied to the system. While this is physically possible, we note that this occurs when the curvature versus saturation curves for drainage exhibit a behavior different from that for imbibition (see Figure 7). This behavior is probably not well described by the current parameter set in equation (36), given the correlation between these fitted parameters.

4. Discussion

We have attempted to show that the free energy in two phase flow may be expressed as a linear combination of seven geometrically independent intrinsic volumes: a saturation, two surface areas, two Euler characteristic, the integrated mean curvature of a fluid phase, and the length of the three-phase contact lines.

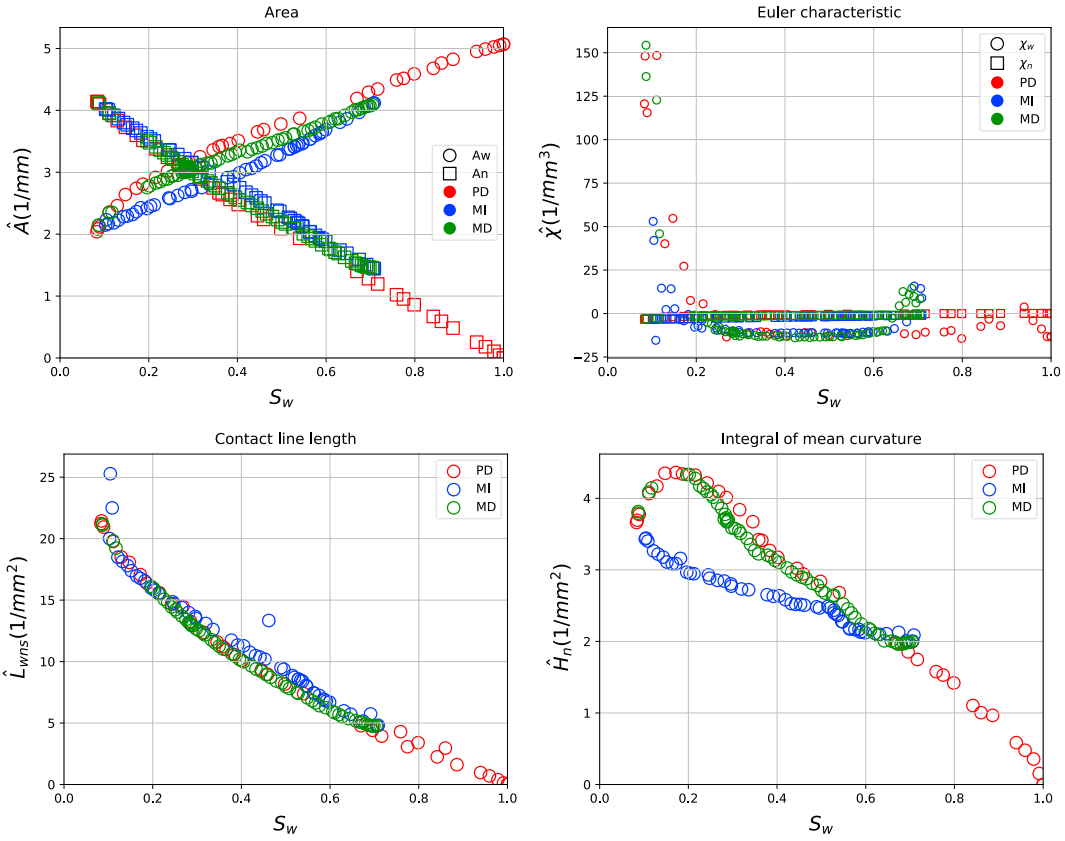

Figure 7. The specific intrinsic volumes area ($\widehat{A}_n$ and $\widehat{A}_w$), integral of mean curvature ($\widehat{H}_n$), Euler characteristic ($\widehat{\chi}_n$ and $\widehat{\chi}_w$), and contact line length ($\widehat{L}_{wns}$) for the different flooding cycles.

We assumed a constant energy efficiency for the imbibition processes when conducting a linear regression on the intrinsic volumes to match the externally applied work. Small changes to this efficiency had little impact on our results. The regression indicated strong dependencies between the intrinsic volumes. This could be the result of dependencies between the intrinsic volumes, or because the experimental data set does not cover situations where the intrinsic volumes have nonlinear dependencies. Therefore, we cannot draw a certain conclusion on the number of parameters needed for a comprehensive description of the studied quasi-static multiphase flow experiments.

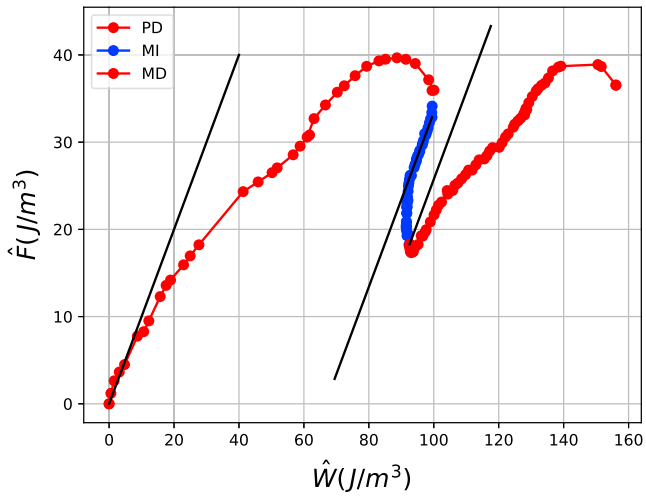

Figure 8. The specific free energy $\widehat{F}$ calculated from the geometrical parameters versus the specific external work $\widehat{W}$ calculated from the saturation change and external pressure difference. The straight lines indicate the reversible processes.

Further analysis of the experimental data revealed that the intrinsic variables other than saturation and areas have a maximum contribution of approximately 20% in the free energy. Linear regression of the free energy as a function of saturation and surface areas only ($S_n, \widehat{A}_n, \widehat{A}_w$) resulted in a worse fit. It also resulted in an unacceptable value for the contact angle, with $\cos\theta < -1$, using equation (38). This contrasts with θ of 43° calculated when all seven variables ($S_n, \widehat{A}_n, \widehat{A}_w, \widehat{H}_n, \widehat{\chi}_n, \widehat{\chi}_w, \widehat{L}_{wns}$) were included in the regression. Therefore, we cannot exclude the variables ($\widehat{H}_n, \widehat{\chi}_n, \widehat{\chi}_w, \widehat{L}_{wns}$) from the geometric description of free energy.

According to the theoretical part of this work, the number of independent geometric variables will never exceed seven. We believe that a deeper approach from thermodynamics is the way forward in identification of possible nongeometrical dependencies. Analysis of more data with less limitation on the temporal resolution may also be helpful in recognizing

the possible nonlinear dependencies between the intrinsic volumes. It should also be noted that studying the physical meaning of the coefficients in equation (14) may lead to a more robust regression and thereby a better predictive capability. This was exemplified for two of the coefficients in the derivation through equation (37)–(45). Furthermore, the thermodynamically constrained averaging theory introduced five geometric variables of nonwetting fluid saturation, nonwetting-wetting and nonwetting-solid interfacial areas, and mean curvatures (Gray & Miller, 2014). In a recent work by McClure et al. (2018), Euler characteristic of the nonwetting fluid is added to the variables introduced in the thermodynamically constrained averaging theory. In this work, the Euler characteristic of both fluids and the length of three-phase contact lines are identified to be independent geometric variables. In addition, our derivations showed that only one integral of mean curvature (of one of the fluids) is independent. At last, we point out that the resulted linear relation of the free energy with the geometric variables is a strong statement supported by the characterization theorem from integral geometry and under the assumptions stated in the theory section (section 2). The description may change to a nonlinear one by discovering possible nongeometric dependencies between geometrically independent variables.

5. Concluding Remarks

Integral geometry was utilized to give a description for free energy of a system of immiscible two-fluid flow based on microscopically evolving variables. The free energy was described as a linear combination of intrinsic volumes of fluids, fluid-fluid and fluid-solid interfaces, and the three phase contact lines. Intrinsic volumes are defined as volumes, surface areas, integrals of mean curvature, and integrals of Gaussian curvature (Euler characteristic) of different domains. We investigated how a number of the intrinsic volumes were related. This helped simplifying the description for energy as a function of the intrinsic volumes and reducing the number of geometrically independent variables to seven with no limiting assumption on wettability. The number of geometrically independent variables for extreme wetting conditions where nonwetting phase has no contact with solid surface was found to be four. The energy of the system was also approximated by a simple thermodynamic approach based on macroscopically measurable variables, assuming that the flow happens very slowly close to hydraulic equilibrium, that is, with low capillary number. By merging these two descriptions of the free energy we found the constant coefficients of the intrinsic volumes for a set of quasi-static experiments. The presented theory also enabled us to estimate the amount of dissipated energy along the imbibition and drainage processes.

Acknowledgments
This work was partly supported by the Research Council of Norway through *Centers of Excellence* funding scheme, project 262644. The experimental data (Schlüter et al. 2016b, 2017b) are available at the URL addresses, https://www.ufz.de/record/dmp/archive/5732/en/ and http://www.ufz.de/record/dmp/archive/4780/en/.

References

Abdallah, W., Buckley, J. S., Carnegie, A., Edwards, J., Herold, B., Fordham, E., et al. (2007). Fundamentals of wettability. *Oilfield Review*, *19*(2), 44–61.

Adamson, A. W., & Gast, A. P. (1997). *Physical Chemistry of Surfaces* (6th ed.). Wiley. Retrieved from https://www.wiley.com/en-us/Physical+Chemistry+of+Surfaces%2C+6th+Edition-p-9780471148739

Armstrong, R. T., McClure, J. E., Berill, M. A., Rücker, M., Schlüter, S., & Berg, S. (2017). Flow regimes during immiscible displacement. *Petrophysics*, *58*(1), 10–18.

Armstrong, R. T., Ott, H., Georgiadis, A., Rücker, M., Schwing, A., & Berg, S. (2014). Subsecond pore-scale displacement processes and relaxation dynamics in multiphase flow. *Water Resources Research*, *50*, 9162–9176. https://doi.org/10.1002/2014WR015858

Avraam, D. G., & Payatakes, A. C. (1995). Flow regimes and relative permeabilities during steady-state two-phase flow in porous media. *Journal of Fluid Mechanics*, *293*, 207–236. https://doi.org/10.1017/S0022112095001698

Bartels, W. B., Rücker, M., Berg, S., Mahani, H., Georgiadis, A., Fadili, A., et al. (2017). Fast X-ray micro-CT study of the impact of brine salinity on the pore-scale fluid distribution during waterflooding. *Petrophysics*, *58*(1), 36–47. SPWLA-2017-v58n1a4

Berg, S., Armstrong, R. T., Georgiadis, A., Ott, H., Schwing, A., Neiteler, R., et al. (2015). Onset of oil mobilization and nonwetting-phase cluster-size distribution. *Petrophysics*, *56*(1), 15–22.

Berg, S., Ott, H., Klapp, S. A., Schwing, A., Neiteler, R., Brussee, N., et al. (2013). Real-time 3D imaging of Haines jumps in porous media flow. *Proceedings of the National Academy of Sciences of the United States of America*, *110*(10), 3755–3759. https://doi.org/10.1073/pnas.1221373110

Darcy, H. (1856). *Les Fontaines Publiques de la Ville de Dijon*. Paris: Dalmont.

Dullien, F. A. L. (1992). *Porous Media Fluid Transport and Pore Structure*. San Diego, CA: Academic Press.

Gray, W. G., & Hassanizadeh, S. M. (1991). Unsaturated flow theory including interfacial phenomena. *Water Resources Research*, *27*(8), 1855–1863. https://doi.org/10.1029/91WR01260

Gray, W. G., & Miller, C. T. (2014). *Introduction to the thermodynamically constrained averaging theory for porous medium systems*. Zürich: Springer. https://doi.org/10.1007/978-3-319-04010-3

Hadwiger, H. (1957). *Vorlesungen über Inhalt, Oberfläche und Isoperimetrie (Lecture on Content, Surface and Isoperimetry)* (p. 312). Berlin-Heidelberg: Springer-Verlag. https://doi.org/10.1007/978-3-642-94702-5

Haines, W. B. (1930). Studies in the physical properties of soil. V. The hysteresis effect in capillary properties, and the modes of moisture distribution associated therewith. *The Journal of Agricultural Science*, *20*(01), 97–116. https://doi.org/10.1017/S002185960008864X

Hassanizadeh, S. M., & Gray, W. G. (1990). Mechanics and thermodynamics of multiphase flow in porous media including interphase boundaries. *Advances in Water Resources*, *13*(4), 169–186. https://doi.org/10.1016/0309-1708(90)90040-B

Hassanizadeh, S. M., & Gray, W. G. (1993a). Towards an improved description of the Physics of two-phase flow. *Advances in Water Resources*, *16*, 53.

Hassanizadeh, S. M., & Gray, W. G. (1993b). Thermodynamic basis of capillary pressure in porous media. *Water Resources Research*, *29*(10), 3389–3405. https://doi.org/10.1029/93WR01495

Herring, A. L., Andersson, L., Schlüter, S., Sheppard, A., & Wildenschild, D. (2015). Efficiently engineering pore-scale processes: The role of force dominance and topology during nonwetting phase trapping in porous media. *Advances in Water Resources*, *79*, 91–102. https://doi.org/10.1016/j.advwatres.2015.02.005

Herring, A. L., Harper, E. J., Andersson, L., Sheppard, A., Bay, B. K., & Wildenschild, D. (2013). Effect of fluid topology on residual nonwetting phase trapping: Implications for geologic CO_2 sequestration. *Advances in Water Resources*, *62*, 47–58. https://doi.org/10.1016/j.advwatres.2013.09.015

Hilfer, R. (1998). Macroscopic equations of motion for two phase flow in porous media. *Physical Review E*, *58*(2), 2090–2096. https://doi.org/10.1103/PhysRevE.58.2090

Hilfer, R. (2006a). Macroscopic capillarity and hysteresis for flow in porous media. *Physical Review E*, *73*(1), 016307. https://doi.org/10.1103/PhysRevE.73.016307

Hilfer, R. (2006b). Capillary pressure, hysteresis and residual saturation in porous media. *Physica A: Statistical Mechanics and its Applications*, *359*, 119–128. https://doi.org/10.1016/j.physa.2005.05.086

Jerauld, G. R., & Salter, S. J. (1990). The effect of pore-structure on hysteresis in relative permeability and capillary pressure: Pore-level modeling. *Transport in Porous Media*, *5*(2), 103–151. https://doi.org/10.1007/BF00144600

Joekar-Niasar, V., Doster, F., Armstrong, R. T., Wildenschild, D., & Celia, M. A. (2013). Trapping and hysteresis in two-phase flow in porous media: A pore-network study. *Water Resources Research*, *49*, 4244–4256. https://doi.org/10.1002/wrcr.20313

Khanamiri, H. H., & Torsæter, O. (2018). Fluid topology in pore scale two-phase flow imaged by synchrotron X-ray microtomography. *Water Resources Research*, *54*, 1905–1917. https://doi.org/10.1002/2017WR021302

Khanamiri, H. H., Torsæter, O., & Voss, G. J. B. (2017). *Fluid topology in drainage and imbibition: Pore scale imaging by synchrotron tomography, SCA2017–085*. Vienna, Austria: International Symposium of the Society of Core Analysts.

Killough, J. E. (1976). Reservoir simulation with history-dependent saturation functions. *Society of Petroleum Engineers Journal*, *16*(01), 37–48. https://doi.org/10.2118/5106-PA

Klain, D. A. (1995). A short proof of Hadwiger's characterization theorem. *Mathematika*, *42*(02), 329–339. https://doi.org/10.1112/S0025579300014625

Leverett, M. C. (1941). Capillary behavior in porous solids. *Society of Petroleum Engineers*, *142*(01), 152–169. https://doi.org/10.2118/941152-G

Liu, Z., Herring, A., Arns, C., Berg, S., & Armstrong, R. T. (2017). Pore-scale characterization of two-phase flow using integral geometry. *Transport in Porous Media*, *118*(1), 99–117. https://doi.org/10.1007/s11242-017-0849-5

McClure, J. E., Armstrong, R. T., Berrill, M. A., Schlüter, S., Berg, S., Gray, W. G., & Miller, C. T. (2018). Geometric state function for two-fluid flow in porous media. *Physical Review Fluids*, *3*, 084306. https://doi.org/10.1103/PhysRevFluids.3.084306

Mecke, K., & Arns, C. H. (2005). Fluids in porous media: A morphometric approach. *Journal of Physics. Condensed Matter*, *17*(9), S503–S534. https://doi.org/10.1088/0953-8984/17/9/014

Mecke, K. R. (2000). *Additivity, convexity, and beyond: Applications of Minkowski functionals in statistical physics*, *Springer Lecture Notes in Physics* (Vol. 554, pp. 111–184). Berlin: Springer. https://doi.org/10.1007/3-540-45043-2_6

Morrow, N. R. (1970). Physics and thermodynamics of capillary action in porous media. *Industrial and Engineering Chemistry*, *62*(6), 32–56. https://doi.org/10.1021/ie50726a006

Niessner, J., Berg, S., & Hassanizadeh, S. M. (2011). Comparison of two-phase Darcy's law with a thermodynamically consistent approach. *Transport in Porous Media*, *88*(1), 133–148. https://doi.org/10.1007/s11242-011-9730-0

Rasband, W. S. (1997–2016). ImageJ. Bethesda, MD: U.S. National Institutes of Health. Retrieved from https://imagej.nih.gov/ij/

Rücker, M., Berg, S., Armstrong, R. T., Georgiadis, A., Ott, H., Schwing, A., et al. (2015). From connected pathway flow to ganglion dynamics. *Geophysical Research Letters*, *42*, 3888–3894. https://doi.org/10.1002/2015GL064007

Schlüter, S., Berg, S., Li, T., Vogel, H.-J., & Wildenschild, D. (2017a). Time scales of relaxation dynamics during transient conditions in two-phase flow. *Water Resources Research*, *53*, 4709–4724. https://doi.org/10.1002/2016WR019815

Schlüter, S., Berg S., Li, T., Vogel, H.-J., & Wildenschild, D. (2017b). Metadata for doi:10.1002/2016WR019815. Retrieved from http://www.ufz.de/record/dmp/archive/4780/en/

Schlüter, S., Berg, S., Rücker, M., Armstrong, R. T., Vogel, H.-J., Hilfer, R., & Wildenschild, D. (2016a). Pore-scale displacement mechanisms as a source of hysteresis for two-phase flow in porous media. *Water Resources Research*, *52*, 2194–2205. https://doi.org/10.1002/2015WR018254

Schlüter, S., Berg, S., Rücker, M., Armstrong, R. T., Vogel H.-J., Hilfer, R., & Wildenschild, D. (2016b). Metadata for doi: 10.1002/2015WR018254. Retrieved from https://www.ufz.de/record/dmp/archive/5732/en/

Seabold, S., & Perktold, J. (2010). Statsmodels: Econometric and statistical modeling with python. In *Proceedings of the 9th Python in Science Conference* (Vol. 57, pp. 57–61). Austin: SciPy Society. Retrieved from http://conference.scipy.org/proceedings/scipy2010/pdfs/seabold.pdf

Singh, K., Menke, H., Andrew, M., Lin, Q., Rau, C., Blunt, M. J., & Bijeljic, B. (2017). Dynamics of snap-off and pore-filling events during two-phase fluid flow in permeable media. *Scientific Reports*, *7*(1), 5192. https://doi.org/10.1038/s41598-017-05204-4

Singh, K., Scholl, H., Brinkmann, M., Michiel, M. D., Scheel, M., Herminghaus, S., & Seemann, R. (2017). The role of local instabilities in fluid invasion into permeable media. *Scientific Reports*, *7*(1), 444. https://doi.org/10.1038/s41598-017-00191-y

Smith, W. O., Foote, P. D., & Busang, P. F. (1931). Capillary rise in sands of uniform spherical grains. *Physics*, *1*(1), 18–26. https://doi.org/10.1063/1.1744981

Tsakiroglou, C., Aggelopoulos, C., Terzi, K., Avraam, D., & Valavanides, M. (2015). Steady-state two-phase relative permeability functions of porous media: A revisit. *International Journal of Multiphase Flow*, *73*, 34–42. https://doi.org/10.1016/j.ijmultiphaseflow.2015.03.001

Vogel, H. J., Weller, U., & Schlüter, S. (2010). Quantification of soil structure based on Minkowski functions. *Computers & Geosciences*, *36*(10), 1236–1245. https://doi.org/10.1016/j.cageo.2010.03.007, Retrieved from www.quantim.ufz.de

Wyckoff, R. D., & Botset, H. G. (1936). The flow of gas-liquid mixtures through unconsolidated sands. *Journal of Applied Physics*, *7*, 325.